

# Enhanced Wastewater Remediation Using Mesoporous Activated Wheat Straw Biochars: A Dye Removal Perspective

Priyanka, Devika Vashisht, Alex O. Ibhaddon, Surinder K. Mehta, and Martin J. Taylor\*

Cite This: <https://doi.org/10.1021/acssusresmgmt.3c00109>

Read Online

ACCESS |

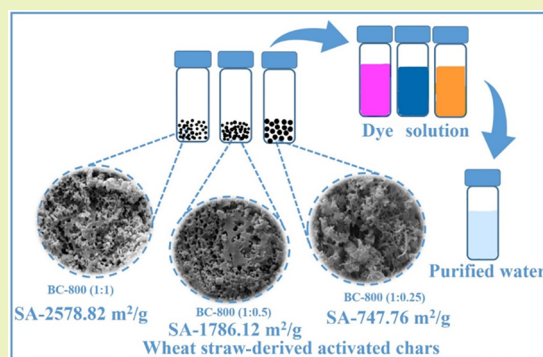
Metrics &amp; More

Article Recommendations

Supporting Information

**ABSTRACT:** The escalating contamination of water bodies by synthetic dyes necessitates innovative and ecoconscious strategies for wastewater treatment. In this study, activated biochars BC-800 (1:0.25), BC-800 (1:0.5), and BC-800 (1:1) from wheat straw were synthesized. Here, ratios denote the mass relationship between wheat straw and potassium hydroxide; “800” represents the pyrolysis temperature. These activated biochars were rigorously characterized revealing the most efficient material, BC-800 (1:1), presenting a surface area of 2578.82 m<sup>2</sup>/g and average pore diameter of 5.51 nm. Across parallel batch experiments, it effectively extracted synthetic dyes (rhodamine B (RhB), methylene blue (MB), and methyl orange (MO)) from wastewater within 15–20 min, primarily through chemisorption pathways. Increased surface area and porosity resulted in a greater dispersion of adsorption sites including C=C linkages ( $\pi$ - $\pi$  interactions) and H-bonding via surface carbonyl groups (C=O). To understand the adsorption mechanism, Langmuir, Freundlich, and Temkin isotherm models were employed to investigate the equilibrium adsorption behavior. Results show that BC-800 (1:1) followed the Freundlich isotherm ( $R^2$ : 0.9659 for RhB, 0.9927 for MB, and 0.9979 for MO, respectively), showing dye molecules form multilayers on the surface of the biochar ( $\pi$ -stacking). Biochar recycling through chemical regeneration demonstrated sustained dye removal efficiency >90% for BC-800 (1:1) over multiple cycles.

**KEYWORDS:** biomass, activated biochar, biorenewable filter, rhodamine b, methylene blue, methyl orange



## 1. INTRODUCTION

Across the globe, the contamination of freshwater through organic and inorganic pollutants has led to a lack of drinkable water. This has been intensified by the rapid surge in the global population, the far-reaching impacts of climate change, and the unabated expansion of industrial activities. Consequently, the simultaneous rise in freshwater users and polluters has significantly contributed to the depletion of a vital resource, drinking water.<sup>1</sup> Among the most notable culprits of industrial pollution are dyes, which have witnessed a substantial surge in usage, including core dyes such as methylene blue (MB), methyl red (MR), congo red (CR), rhodamine B (RhB), methyl orange (MO), and crystal violet (CV). The worldwide textile industry's continual growth is emblematic of this escalating trend, with nearly 10,000 commercial dyes and pigments being produced globally, exceeding an annual production of  $7 \times 10^5$  tonnes.<sup>2</sup> Given that most dyes readily dissolve in water due to their organic salt nature, discharging dye-laden effluents directly into water bodies poses a serious threat to photosynthetic activity and harms aquatic biodiversity. Innovative methods for the extraction of dyes from aqueous solutions have been developed including UV-vis photodegradation processes,<sup>3</sup> advanced oxidation,<sup>4</sup> graphene derivatives,<sup>5</sup> electro-Fenton,<sup>6</sup> and ultrasonic methods.<sup>7</sup> How-

ever, due to their high cost, limited efficiency, and sludge disposal requirements, the majority of these procedures are not practical to deploy at an industrial scale.<sup>8</sup> Therefore, there is a critical need to develop an efficient, environmentally acceptable method for removing colors from industrial wastewater. Adsorption is utilized extensively for the elimination of colors from aqueous solutions and is acknowledged as the most flexible approach employed in developing nations.<sup>9,10</sup> The exertion of agricultural waste in the preparation of adsorbents makes the procedure commercially viable and appealing for scaling up, especially for countries with high agricultural activities and or large producers of lignocellulosic biomass waste.<sup>11,12</sup>

Over the past five decades, agricultural production has tripled due to expanded agricultural lands, the transformative green revolution, and rapid global population growth. To combat environmental pollution and boost waste recycling,

**Received:** November 21, 2023

**Revised:** January 26, 2024

**Accepted:** January 26, 2024

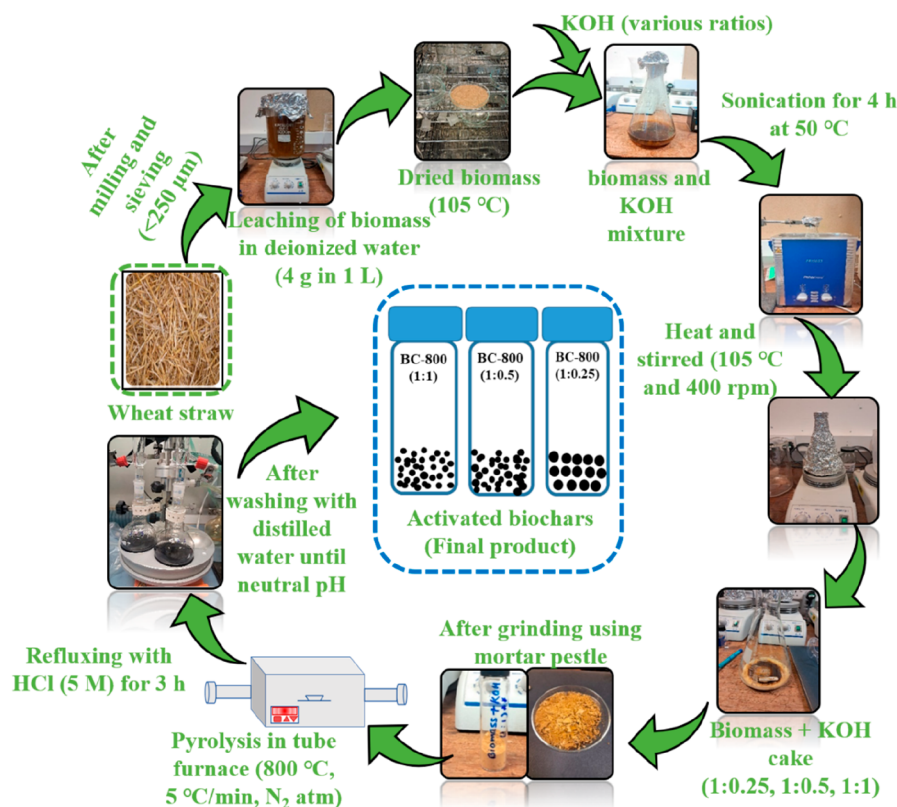


**Figure 1.** Step-by-step synthetic procedure to create activated biochars from wheat straw. The dashed green line indicates the process starting point, and the dashed blue line is the product.

researchers utilize lignocellulosic biomass residues to produce biochar-based materials, capitalizing on their significant surface area and porosity through the appropriate activation processing. Biochars have become a preferred option for dye removal in water solutions due to their carbon neutral and sustainable credentials.

To enhance the sorption performance of biochar, dehydrating and/or oxidizing substances, such as KOH,  $\text{K}_2\text{CO}_3$ , NaOH,  $\text{Na}_2\text{CO}_3$ , including acids  $\text{H}_3\text{PO}_4$  and  $\text{H}_2\text{SO}_4$ , and  $\text{ZnCl}_2$ , have been discussed for the formation of activated carbons and biochars.<sup>13–16</sup> The most effective of them was found to be potassium hydroxide (KOH), it was found that through KOH activation, a microporous activated carbon can be produced with the development of  $-\text{OH}$  functional groups on the carbon surface.<sup>17</sup> Recently, KOH has been used to activate *Enteromorpha prolifera* biochar with a specific surface area of  $1262.8\ \text{m}^2/\text{g}$ .<sup>18</sup> Additionally, a significant biochar surface area ( $3164\ \text{m}^2/\text{g}$ ) has been reported by pyrolyzing waste litchi shells after a KOH pretreatment.<sup>19</sup> However, there is limited information on the application of such “super chars” for the removal of dyes such as RhB, MB, and MO from wastewater. Hence, RhB, MB, and MO have been selected as exemplars with different net charges, shape, and chemical structures to determine if activated “super chars” are an effective and rapid method of dye removal, capable of outperforming conventional char production routes.<sup>20,21</sup>

In this study, we have developed a method of producing large-surface area biochars derived from wheat straw using varying KOH ratios (1:0, 1:0.25, 1:0.5, 1:1, 1:1.5, and 1:2) as an activator and investigate the sorption efficiency of this family of materials through the extraction of MO, MB, and

RhB from wastewater. Subsequently, the produced activated biochars are characterized quantitatively and qualitatively using a range of techniques, including SEM, TGA, CHN, ATR-FTIR, nitrogen physisorption, and PXRD. The investigation further delves into exploring the effects of variables such as adsorbent dosage, initial dye concentration, contact time, pH, and adsorption kinetics on the activated biochar’s performance for dye removal. Additionally, this study utilizes the Langmuir, Freundlich, and Temkin isotherm models to gain a deeper insight into the adsorption behavior of the activated biochars for the selected dyes. By employing a straightforward and practical experimental approach, this research presents an avenue to fully harness the potential of biomass-derived activated carbons for wastewater treatment that can be scaled up sustainably and applied to real world applications.

## 2. MATERIALS AND METHODS

**2.1. Chemical Reagents.** Wheat straw was locally sourced from the Humber Estuary region in East Yorkshire, United Kingdom. Ethanol (absolute), acetone ( $\geq 99.8\%$ ), and hydrochloric acid ( $\sim 37\%$ ) were from Fisher Chemicals. RhB ( $\text{C}_{28}\text{H}_{31}\text{ClN}_2\text{O}_3$ ) ( $\geq 95\%$ ), MB ( $\text{C}_{16}\text{H}_{18}\text{ClN}_3\text{S}$ ) ( $\geq 95\%$ ), and MO ( $\text{C}_{14}\text{H}_{14}\text{N}_3\text{NaO}_3\text{S}$ ) were purchased from Sigma-Aldrich. Sodium hydroxide pellets (98%) and potassium hydroxide (KOH) were obtained from Thermo Scientific Chemicals. All of the experiments were performed in deionized water. Analytical grade reagents were employed without any further purification or drying.

**2.2. Preparation of Biochar.** Wheat straw waste biochars were synthesized via slow pyrolysis. Initially, the waste stream was physically pretreated by knife mill (Retsch GM 200 Grindomix), followed by size selection (Retsch AS200 vibratory sieve shaker), where the  $<250\ \mu\text{m}$  fraction was water washed (physicochemical leaching) in deionized water at room temperature in a ratio of 10 g/L

for 24 h, followed by filtering and drying in a Fisherbrand convection oven at 105 °C.<sup>22</sup> Prior to pyrolysis, the dried biomass was mixed with the desired mass of KOH, where the mass of wheat straw to KOH varied. These ratios were 1:0, 1:0.25, 1:0.5, 1:1, 1:1.5, and 1:2 where mixing took place in 100 mL of deionized water and sonicated using a Fisherbrand S-Series heated ultrasonic bath at 50 °C for 4 h. Here, hydrolysis occurred liberating cellulose and hemicellulose from the lignin backbone, as well as embedding potassium cations into the physical wheat straw matrix.<sup>23</sup> The mixture was then heated to ~105 °C on a hot plate and stirred to drive off the water. The resulting yellowish cake was pyrolyzed in a tube furnace at 800 °C under a nitrogen atmosphere at 5 °C/min and held for 1 h. The resulting biochar was washed with ethanol and acetone (100 mL) to eliminate bio-oil/tar residues liberated during the pyrolysis reaction (until the washings transitioned from yellow to completely colorless). After the biochars were dried at 105 °C to ensure the removal of solvents, the biochars were refluxed in 5 M HCl for 3 h to digest the impregnated potassium as well as other digestible ash components. The final product was thoroughly washed in deionized water until a pH of 7.0 was obtained in the effluent; this was followed by drying in an oven at 105 °C. As a benchmark material following on from previous work reported,<sup>22</sup> a conventional biochar produced at 800 °C with no other postprocessing was generated (BC-800 (1:0)) to understand the structural effects of activation. According to various biomass to KOH ratio, the samples were named BC-800 (1:0), BC-800 (1:0.25), BC-800 (1:0.5), BC-800 (1:1), BC-800 (1:1.5), and BC-800 (1:2). Figure 1 illustrates the stepwise procedure to design the activated biochars using wheat straw, as mentioned above.

**2.3. Characterization of Solid Samples.** Fourier transform infrared (FTIR) spectra of samples were collected using a Thermo Scientific Nicolet iS5 instrument with a PIKE MIRacle single reflection horizontal diamond ATR accessory (600–4000 cm<sup>-1</sup>). Thermogravimetric analysis was carried out on the parent wheat straw feedstock using a LECO 701 thermogravimetric analyzer (~1.00 g scale) using the method mentioned in our previous work.<sup>22</sup> Biochar ash loading was determined using a Mettler Toledo TGA/DSC 1 (~10 mg) in air at 30 mL/min, with a ramp rate of 10 °C/min from room temperature to 750 °C, holding for 1 h. Ultimate analysis for the parent feedstocks and biochars were acquired using a Fisons Instruments EA 1108 CHNS elemental analyzer. A scanning electron microscopy was conducted using a Zeiss EVO 60 at 10<sup>-2</sup> Pa with a 20 kV electron acceleration voltage. Samples were adhered to a conductive carbon tape and Au coated to increase the image contrast. Prior to nitrogen physisorption, samples were degassed for 3 h at 110 °C with a nitrogen capillary feed and subsequently analyzed individually using a Micrometrics TriStar porosimeter to quantify the available surface area and overall porosity. Powder X-ray diffraction (PXRD) measurements were acquired using monochromated Cu K $\alpha$  radiation ( $\lambda = 0.1542$  nm) on a PANalytical Empyrean series 2 diffractometer. Subsequent analysis of the diffractograms was performed in HighScore Plus (2013, PANalytical B.V.) with the ICDD's PDF-2 2012 database.

**2.4. Characterization of Liquid Samples.** RhB concentration was measured using a Jenway 7315 UV-Vis spectrophotometer at 554 nm using a 3.5 mL quartz cuvette with a 1 cm<sup>3</sup> path length. The resultant calibration plot for RhB is illustrated in Figure S1a, demonstrating a high level of experimental accuracy with a coefficient of determination ( $R^2$ ) of 0.99782. Similarly, for MB, a calibration plot was generated across a range of eight concentrations by measuring the concentration of the solution through its distinctive peak at 664 nm over various dilution factors. The resulting calibration plot, shown in Figure S1b, showed a strong correlation with a  $R^2$  value of 0.99669. In the case of MO, its concentration was determined using a wavelength of 465 nm. Figure S1c displays a strong correlation between the UV peak of MO and its concentration, as evidenced by the high  $R^2$  value of 0.9992 across a range of seven concentrations.

**2.5. Sorption Experiments.** A comprehensive series of batch adsorption studies were carried out in triplicate to investigate the adsorption behavior of dyes on structured, activated biochars, exploring the initial concentration, contact time, adsorbent dose,

and initial pH. Triplicate uptake experimentation was followed to minimize error in analysis, be this caused by spectrophotometer signal variation, dose variations, and or amount of biochar temporarily removed between sampling. To initiate the experiments, stock solutions of RhB, MB, and MO at 100 mg/L concentrations were prepared and subsequently diluted to achieve desired concentrations ranging from 5 to 40 mg/L, utilizing borosilicate glass vials (20 mL). The pH values of the solutions were adjusted and maintained through the use of 0.1 M HCl and 0.1 M NaOH, facilitated by a Fisherbrand HydruS 300 pH meter. To assess dye adsorption, a known quantity of the activated biochar adsorbents was introduced to the dye solution, followed by magnetic stirring at 500 rpm and room temperature. The initial test of the biochar with no activation (BC-800 (1:0)) as a benchmark material demonstrated a low efficiency in removing the organic contaminants, yielding removal rates of 25.83% for RhB, 29.92% for MB, and 35.76% for MO over 150 min. Consequently, subsequent experiments were conducted using BC-800 (1:0.25), BC-800 (1:0.5), and BC-800 (1:1). Although two further materials were developed using a higher KOH ratio, due to their rapidly decreasing surface areas (Table 1) and collapsed structures, they were omitted from testing.

**Table 1. BET Surface Area, Pore Size, and Pore Volume Analysis of Inactivated (BC-800 (1:0)) and Activated Biochar Samples (BC-800 (1:0.25), BC-800 (1:0.5), BC-800 (1:1), BC-800 (1:1.5), and BC-800 (1:2))**

Biochar	BET surface area (m <sup>2</sup> /g)	Pore size (nm)	Pore volume (cm <sup>3</sup> )
BC-800 (1:0)	32.10 ± 0.51	–	–
BC-800 (1:0.25)	747.76 ± 16.58	6.48	0.16
BC-800 (1:0.5)	1786.12 ± 37.63	6.42	0.36
BC-800 (1:1)	2578.82 ± 53.33	5.51	0.49
BC-800 (1:1.5)	1444.66 ± 29.99	7.40	0.40
BC-800 (1:2)	1283.55 ± 26.53	6.95	0.37

For kinetic studies, samples were withdrawn at time intervals of 0, 1, 3, 5, 7, 10, 15, 20, 30, 40, 50, 60, 80, 100, 120, 150, 180, 210, and 270 min. For these measurements, 2 mL of the suspension was centrifuged by using a Fisher Scientific centrifuge (12 V DC) at 6000 rpm for 5 min, resulting in the separation of the adsorbent from the solution. The concentration of the dye in the filtrate was determined by using a UV-vis spectrophotometer. Following the analysis, the liquid and adsorbent were reintroduced back into the mixing vessel to ensure continuous assessment of the dye adsorption process.

For dose studies, biochar masses of 2, 3, 5, 6, 8, 10, 12, and 14 mg were added to 20 mg/L of each dye (RhB, MB, and MO) with a fixed pH of 6 for RhB and MO, and while pH 8 was used for MB, the choice of pH for these measurements was validated during the extraction optimization process. The same procedure was used to study the effect of dye concentration (5, 10, 15, 17.5, 20, 22.5, 25, 30, 35, and 40 mg/L), where the optimized pH for each dye was used.

**2.6. Biochar Reusability.** To investigate the long-term sustainability and regeneration of the activated biochar adsorbents, after dye extraction, the BC-800 materials were refluxed in ethanol (EtOH, 50 mL) for 0.5 h, followed by separating and drying under *vacuo*, where two washes of EtOH (10 mL) were used to ensure there was no further dye release (colorless eluant). The regenerated biochars were then dried for further use in a convection oven for 2 h at 105 °C. This process was completed five times for each biochar, across each dye investigated.

## 3. RESULTS AND DISCUSSION

**3.1. Physical Properties of Feedstock and Biochars.** Figure S2 shows the N<sub>2</sub> adsorption–desorption isotherm and pore size distributions of the activated biochars. The resulting isotherms applied to these plots were confirmed as Type IV, as shown in Figure S2a, along with pore size distributions,

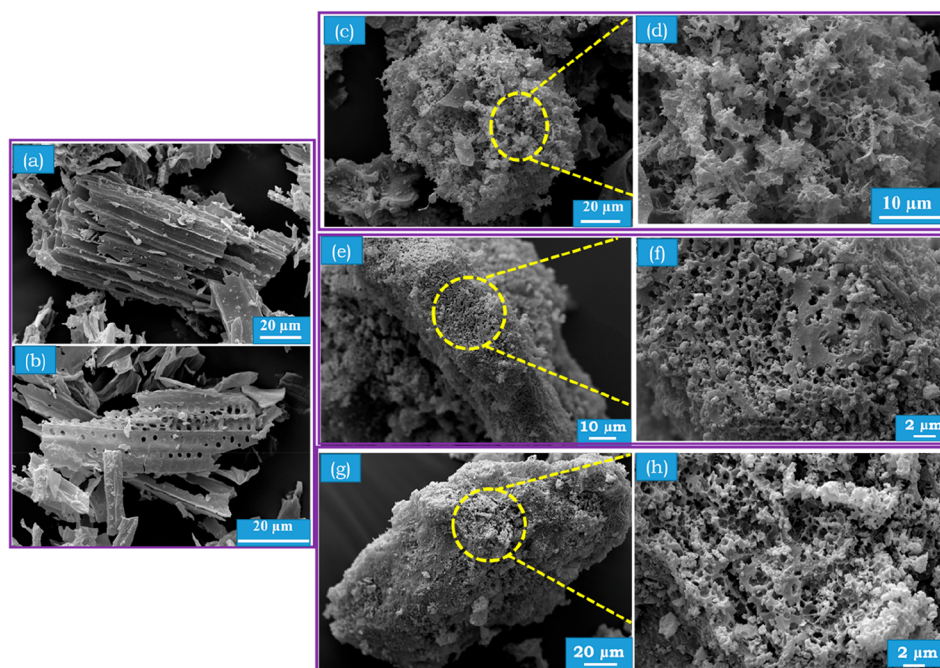


**Figure 2.** SEM micrographs of the base biochar without activation (a, b) BC-800 (1:0) as well as activated biochars, with (c, d) BC-800 (1:0.25), (e, f) BC-800 (1:0.5), and (g, h) BC-800 (1:1).

suggesting that the biochar adsorbents have pore sizes in the range of 2–50 nm, confirming them to be mesoporous. Table 1 shows the BET surface area of BC-800 (1:0) is  $32.10 \pm 0.51 \text{ m}^2/\text{g}$ ; then following activation, the BET surface area increases from  $747.76 \pm 16.58 \text{ m}^2/\text{g}$  for BC-800 (1:0.25) to  $2578.82 \pm 53.33 \text{ m}^2/\text{g}$  for BC-800 (1:1). However, the available surface area was found to decrease from  $2578.82 \pm 53.33 \text{ m}^2/\text{g}$  (1:1) to  $1444.66 \pm 29.99$  (1:1.5) and  $1283.55 \pm 26.53 \text{ m}^2/\text{g}$  when the mass ratio increased to 1:2. This suggests that 1:1 is the optimal mass ratio to maximize the available adsorbent surface area and the highest pore volume ( $0.49 \text{ cm}^3$ ). The rapid reduction in available surface area and pore volume as the KOH to wheat straw mass ratio exceeds 1:1 is clearly shown in Figure 2 where the pore structure appears to start to collapse (formation of larger voids). This change in structure is caused by the increase in voids generated after KOH digestion; these then collapse into one and other, generating larger cavities, evidenced in Table 1 by an increase in pore diameter from 5.5 to  $\sim 7.0 \text{ nm}$ , shown by BC-800 (1:1.5) and BC-800 (1:2).<sup>24,25</sup> As a result of this clear structural collapse, these mentioned biochars were not trialed for dye extraction, as their textural properties are lower than BC-800 (1:0.5).

Figure S2b shows the pore size distribution plots for biochar samples, which clearly indicate that pores are largely below 5 nm. The average particle sizes for BC-800 (1:0.25), BC-800 (1:0.5), and BC-800 (1:1) are 6.48, 6.42, and 5.51 nm, respectively, while the pore volume of BC-800 (1:1) is  $0.49 \text{ cm}^3$ , which is 3 times the pore volume of BC-800 (1:0.25). KOH activation has therefore been shown to promote the creation of mesoporous biochar.

Thermogravimetric analysis presents the weight loss and derived weight loss (DTG) curves for the leached wheat straw parent material in Figure S3. The main volatile zone occurred between 270 and 350 °C, providing two distinct peaks. The first peak at 272.58 °C is characteristic of hemicellulose depolymerization, and the section at 339.42 °C is seen as the

thermal degradation of cellulose and remaining hemicellulose.<sup>26</sup>

The physical properties (proximate and ultimate analysis) of the leached parent feedstock and biochar samples across all wheat straw:KOH ratios are shown in Table S1. The moisture content of the parent feedstock was found to be 2.91 wt %, after drying which is below the 10 wt % upper recommendation for efficient pyrolysis.<sup>27</sup> The ash content for the parent feedstock, after leaching, was found to be 3.33 wt %, and the subsequent ash loadings for the biochars post (KOH impregnation and pyrolysis) were found to increase up to 17.12 wt %. This value is close to the ash value of the biochar without KOH treatment of 16.93 wt %. This suggests that there are no residues remaining from the KOH treatment after the acid digestion step. Table S1 also illustrates the elemental composition of the parent feedstock and the produced biochars. As anticipated, the carbon content increases following the pyrolysis process (reduction in oxygen). The carbon contents for BC-800 (1:0) and BC-800 (1:1) are 71.58% and 67.94%, and during the KOH hydrolysis process, it is expected that some of the carbon from the sugar components (cellulose and hemicellulose) will be lost as  $\text{CO}_2$  which will have a mild effect on the overall carbon value of the feedstocks, prior to pyrolysis.<sup>28</sup> The hydrogen content experiences a notable reduction due to dehydration that occurs in the cellulose and hemicellulose at higher KOH concentrations. The thermal processing also leads to the removal of surface hydroxyl ( $-\text{OH}$ ) groups, including water, and contributes to the structural breakdown of cellulose. Concurrently, volatilization takes place, fostering decarboxylation and carbon atom condensation within aliphatic systems (generation of  $\text{C}=\text{C}$  and  $\text{C}\equiv\text{C}$  entities), as well as facilitates the generation of aromatic frameworks.<sup>29</sup>

The development of high surface area biochars (Table 1) with a coral-like structure was elucidated through the use of scanning electron microscopy (SEM), shown in Figure 2. The

SEM images of the biochars before activation are shown in Figure 2a and b, presenting two independent grains at similar magnification. It was found that the inactivated biochar had a smooth, fibrous structure, with no observable mesoporous/microporous structure, with the exception of surface perforations (Figure 2b) which are considered to be generated through leaching (water washing prior to pyrolysis) and thermal processing.<sup>30</sup> BC-800 (1:0) presented itself as irregular rods and stalk stems, which is in accordance with the literature.<sup>31</sup> This demonstrated that the wheat straw's structural features were mostly unaltered through the carbonization procedure, resulting in a limited number of pores, evidenced by Table 1 which shows a mostly bulk material with a low available surface area. This agrees with the wider literature, which has found that when pyrolyzing at 800 °C, a heterogeneous surface with some established pores is established, albeit without any distinct shape.<sup>32</sup> However, it can be clearly seen that after chemical activation (Figure 2c–h), the morphological characteristics have substantially changed. The smooth surface of the biochar has been replaced with a disordered shape with a coral-like structure, producing a granular, rough, and uneven pleated surface at low magnification (Figure 2c, e, and g). At higher magnification (Figure 2d, f, and h) the biochar has been heavily structured, resembling coral, subject to the KOH dosage used in the prepyrolysis processing. At a lower ratio (1:0.25, Figure 2d), there is the evidence of some microstructure forming. This is more noticeable in Figure 2e and f (1:0.5) as the structure is observable at both low and high magnification; this material was found to have an available surface area of 2.39 times higher than the biochar shown in Figure 2c and d. For the biochar with the highest reported surface area (1:1), Figure 2g and h shows a highly porous material where there are signs of larger voids forming, showing that the structure is beginning to collapse. Here, there is a range of macropore openings along the surface of the biochar that appear to develop into cavities deeper into the material. This increase in surface decoration (cavities) is evidenced by its increase in available surface area, 1.44 times higher than the 1:0.5 biochar, 3.45 times higher than the 1:0.25 biochar, and 80.33 times higher than the base biochar shown in Figure 2a and b.

In this study, KOH was used as part of the chemical activation process, where the base first hydrolyzed the cellulose and hemicellulose sugars (eqs 1–3) before the K<sup>+</sup> ions were impregnated into the wheat straw matrix as a sacrificial templating agent (eq 4). The activation mechanisms are shown as follows:<sup>33,34</sup>



The etching of C atoms (eqs 1 and 2) were used to achieve deep apertures (Figure 2f and h). At temperatures >600 °C, the generated metallic K is mobile within the matrix and contributes to pore expansion. The porous structure of the wheat straw samples was then further enhanced by the efficient intercalation of the as produced K<sub>2</sub>CO<sub>3</sub> into the wheat straw during carbonization at higher temperature (eq 3). Following complete KOH consumption, metallic K, K<sub>2</sub>O, CO<sub>2</sub>, and CO were formed as shown in eqs 3 and 4, which significantly

reduced the K<sub>2</sub>O and K<sub>2</sub>CO<sub>3</sub> that had been created >700 °C. By refluxing with HCl and repeatedly washing with distilled water until the pH was neutralized, salt (KCl) and excess KOH were removed, among the removal of other ash-based entities that could be present such as Na, Mg, and Ca which have been found in the past to be present in wheat straw.<sup>35</sup>

The infrared spectra of the biochar samples are shown in Figure 3. Across the board, the functional groups observed

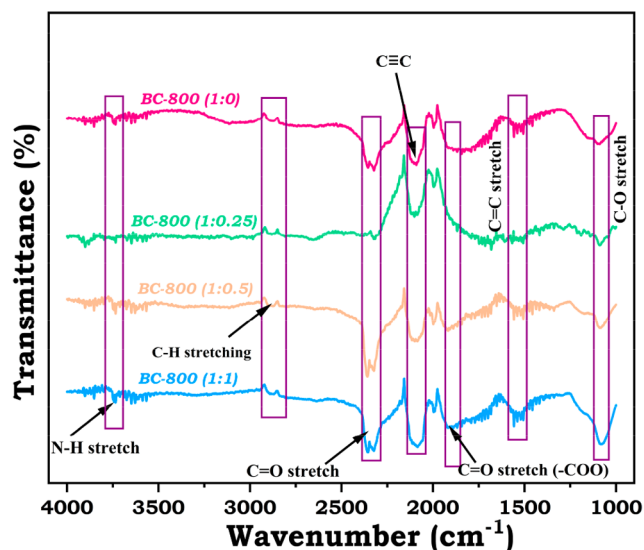
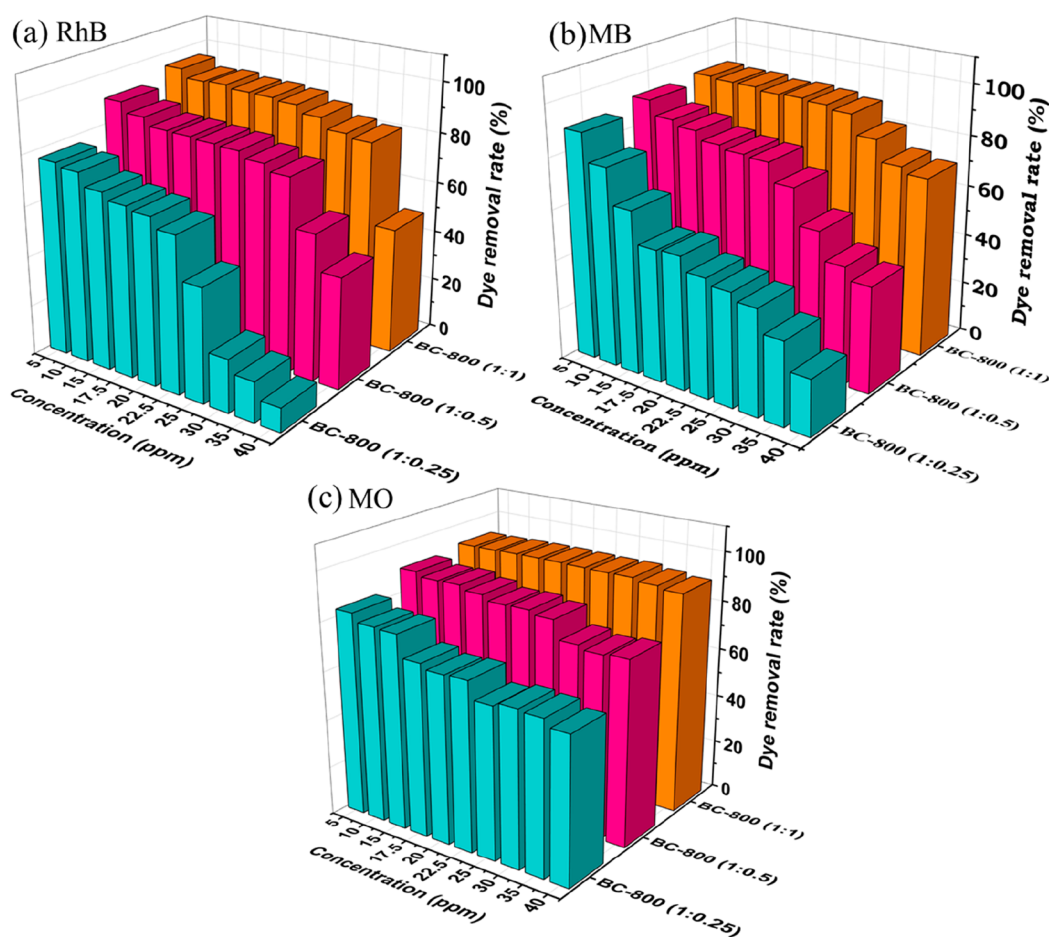


Figure 3. Attenuated total reflectance-Fourier transform infrared spectroscopy of inactivated and activated biochar samples.

were similar, irrespective of activation or not where only the intensities varied; this aspect is subject to the sample holder and sample interaction with the diamond ATR. It was found that there was a peak ~3738 cm<sup>-1</sup>, which was attributed to N–H stretching vibrations. This is observable for the biochars due to the pyrolysis process taking place in a N<sub>2</sub> atmosphere, as shown in Table S1 where the nitrogen content was found to subtly increase after thermal processing. Postpyrolysis, there appears to be still some aromatic compounds present in the lignin where a C=C stretch was observable at 1525 cm<sup>-1</sup>. Additionally, the peak at 1073 cm<sup>-1</sup> is assigned to alcohol stretching vibrations, which are present in the hydroxycinnamyl alcohols that build the lignin regions of the samples.<sup>23</sup> The peak at 2875 cm<sup>-1</sup> denotes the C–H stretching vibration in the aromatic methoxyl groups of lignin as well as the methyl (–CH<sub>3</sub>) and methylene (–CH<sub>2</sub>) side chains that are still present. At 2106–2087 cm<sup>-1</sup>, the samples showed evidence of C≡C in aromatic compounds or can also be associated with the stretching vibration of conjugated carbon–carbon double bonds (C=C) in aliphatic chains, often referred to as Lewis acid sites; it has been found that these regions are thermally induced and are therefore a product of the pyrolysis at 800 °C.<sup>36</sup> The area from around 2350 to 2315 cm<sup>-1</sup> represents C=O stretching ketenes.<sup>37–39</sup> The peak at 1911 cm<sup>-1</sup> is linked to the stretching vibration of the carbonyl group (C=O) in carboxylate ions.

The crystallinity of inactivated and activated biochars was characterized by PXRD. Due to the use of low sample quantities, a zero-background sample holder was used where the biochar was adhered to the surface using a small amount of vacuum grease. The grease was found to generate a level of



**Figure 4.** Effect of initial dye concentration on the removal rate of dyes (a) RhB, (b) MB, and (c) MO (initial concentration of 5–40 mg/L, pH 6 for MO and RhB, pH 8 for MB, dose of 6 mg).

constructive interference, which created a signal at  $12.0^\circ$ , as shown in Figure S4. This appears as a shoulder on the amorphous carbon signal shown at  $22.5^\circ$ , which is expected for the biochar material. In addition to this, a low intensity signal at  $43.4^\circ$  was seen which has previously reported the development of graphite with an amorphous carbon turbostratic structure. The absence of any further signals is a sign that the acid postprocessing and subsequent washing is effective to remove noncarbon components, namely, potential contaminants such as KOH, KCl, and  $K_2CO_3$ . Furthermore, the near identical PXRD diffractograms for all of the samples show that KOH activation had minimal effect on sample graphitization.<sup>40,41</sup>

**3.2. Batch Adsorption Studies.** Depending on the porous nature and functional groups available on the surface of the biochar (Figure 3), we assessed the effectiveness of activated biochars BC-800 (1:1), BC-800 (1:0.5), and BC-800 (1:0.25) for the removal of the three organic dye molecules, RhB, MB, and MO from water. Through a series of dye adsorption tests, the viability of employing activated biochars in wastewater purification was determined. The adsorbents were added to the aqueous dye solution and stirred at room temperature with constant stirring (500 rpm). As a result, the dyes were able to adhere to the materials' surfaces (interior pore structure and exterior biochar superstructure) via electrostatic contact. The dye-loaded biochars were sub-

sequently centrifuged to separate the biochars from the mixture, and the liquid samples were extracted for the measurement of absorbance at a maximum wavelength ( $\lambda_{\max} = 554$  nm for RhB,  $\lambda_{\max} = 664$  nm for MB, and  $\lambda_{\max} = 465$  nm for MO), which allowed for the calculation of the residual dye concentration in solution. To check the accessibility of the biorenewable materials for dye removal, various effective parameters such as pH, dosage, contact time, and dye concentration were examined at room temperature.

**3.2.1. Effect of pH on Adsorption Capacity.** Figure S5 depicts the influence of pH on the adsorption capacity. The pH of the solution was found to have an impact on both the degree of protonation of the functional groups and, subsequently, the surface charge of biochars.<sup>42</sup> The adsorption tests were carried out with a 20 mg/L dye solution at different pHs ranging from 2–12, maintaining the acidity/basicity using 0.1 M HCl and 0.1 M NaOH.

For RhB, the biochar dose amount of 6 mg at a concentration of 20 mg/L was used to determine the optimum pH value to use to achieve the maximum removal rate. This was found to be pH 6 with 95.52% for BC-800 (1:1), 94.26% for BC-800 (1:0.5), and 64.86% for BC (1:0.25), although BC-800 (1:1) showed the removal rate to be above 90% for all pHs except pH 12, as depicted in Figure S5a, dropping to 78.08%. For rhodamine B, there are two species in solution: the cationic form and the zwitter ionic form. The cationic form is

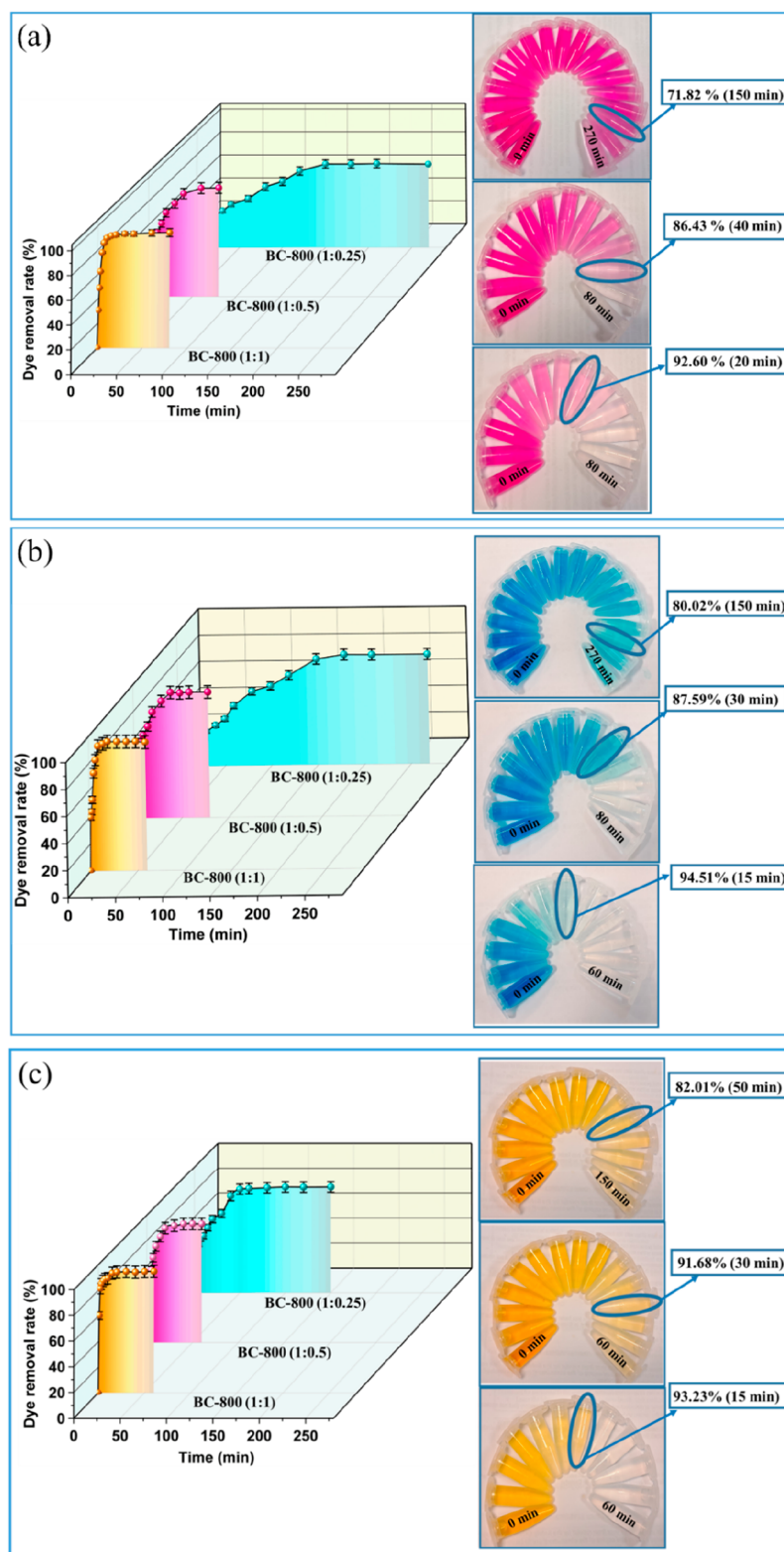


**Figure 5.** Effect of contact time on dye removal rate for (a) RhB, (b) MB, and (c) MO using activated biochars. Blue circles highlight the points of maximum uptake (initial concentration, 20 mg/L; pH 6 for MO and RhB; pH 8 for MB).

found dominantly in acidic solutions, while at higher pH, RhB exists as the zwitter ionic form and forms dimers with varying geometries (H and J dimers, subject to  $\pi$  interactions in the xanthene cores), increasing the overall size of the dye molecule.<sup>43</sup> As a result, the adsorbent's pores would become

blocked due to accumulation of larger molecular structures exceeding 32 angstroms (3.2 nm).<sup>44</sup>

For MB, the same dose amount of 6 mg at a concentration of 20 mg/L was considered to evaluate the optimum pH value. The maximum removal efficiency was attained at pH 8, with

93.25% for BC-800 (1:1), 90.43% for BC-800 (1:0.5), and 72.53% for BC-800 (1:0.25) within 15, 40, and 120 min (Figure S5b). Poor removal occurs at low pH due to competition between the solution's  $H^+$  ions and  $MB^+$ , a cationic organic dye found in water.<sup>22</sup> The surface of the biochar deprotonates as the pH rises, which is advantageous for electrostatically adsorbing the cationic MB dye. At higher pH, the oxygenated functional groups such as hydroxyl and carboxyl groups in biochars could be easily deprotonated, leading to a favorable electrostatic attraction with the cationic MB.<sup>45</sup>

Finally, the same dose and concentration was used for MO. The efficiency of adsorption was found to be 95.12% for BC-800 (1:1), 95.79% for BC-800 (1:0.5), and 84.13% for BC-800 (1:0.25) at an acidic pH 2, steadily declining as the pH increased, as shown in Figure S5c. In the pH range of 6–8, the removal efficiency was 93.74% for BC-800 (1:1), 92.00% for BC-800 (1:0.5), and 74.65% for BC-800 (1:0.25); however, after this it reduced. Thus, pH 6 was found to be the ideal pH for adsorption tests. In acidic circumstances, a high removal efficiency can be attained because the negatively charged adsorption sites on the adsorbent surface protonate, and there are stronger electrostatic interactions between the anionic dye molecules and the adsorbent surface.<sup>46</sup>

**3.2.2. Effect of Dose on Adsorption Capacity.** The dosage employed in the study is one of the crucial factors in the adsorption process and its direct applicability as a usable technology at scale. The adsorption of dyes was investigated by varying the dose from 2–14 mg at ambient temperature with an initial concentration of 20 mg/L, maintaining pH 6 for RhB and pH 8 for MO and MB in a glass vial, and stirred continuously at 500 rpm. Figure S6 exemplifies the effect of biochar dosage on the dye removal efficiency. It was found that increasing the dose from 2 to 6 mg, the dye removal rate improved, while no change was further observed on increasing the dose. The cause is that a higher biochar dosage increased the number of surface adsorption sites, which led to a higher amount of adsorption. By further increasing the biochar dosage, it was found that there was no beneficial effect for BC-800 (1:1), and the excess in available adsorption sites was not utilized.<sup>47,48</sup> For the case of 6 mg of BC-800 (1:1), this material exhibited a removal efficiency of 94.42%, while 8 mg of BC-800 (1:0.5) and BC-800 (1:0.25) presented removal efficiencies of 90.13% and 73.11%, respectively, for RhB, while for MB, 6 mg of each adsorbent provided removal efficiencies of 91.66%, 89.91%, and 75.95% for BC-800 (1:1), BC-800 (1:0.5), and BC-800 (1:0.25), respectively. Finally, for MO, 6 mg of the coral-structured adsorbents demonstrated dye removal of 95.73%, 84.03%, and 71.23% for BC-800 (1:1), BC-800 (1:0.5), and BC-800 (1:0.25), respectively.

**3.2.3. Effect of Initial Dye Concentration on Adsorption Capacity.** A series of batch experiments were carried out for concentration studies using 10 different aliquots of concentrations varying from 5–40 mg/L for each dye. Each dye solution was dosed with the optimum mass of activated biochars, with the prime pH value mentioned previously for each dye.

The adsorption performance of the coral-structured biochars is shown in Figure 4. At 5 mg/L, for BC-800 (1:1), the removal efficiency was observed to be 95.50% for RhB, 93.34% for MB, and 92.50% for MO, respectively. However, at 40 mg/L for the same dyes, 49.64%, 70.98%, and 90.20% removal rates were observed; this shows that the biochars are effective

at removing MO at an efficiency >90% at a higher concentration, utilizing 6 mg of adsorbent. Similarly, at a higher concentration, there is a decrease in RhB and MB adsorption due to limitation for adsorption or pore blockages. Similar results were seen for BC-800 (1:0.5), where removal efficiencies for RhB, MB, and MO at 5 mg/L were 90.77%, 92.36%, and 90.60%, while at 40 mg/L, the removal rates were found to decrease to 44.13%, 41.98%, and 75.49%. Finally, for the activated biochar with the lowest surface area and porosity (BC-800 (1:0.25)), the removal efficiencies for RhB, MB, and MO at 5 mg/L were 77.01%, 89.33%, and 83.49%, whereas at 40 mg/L, removal rates of 9.63%, 22.21%, and 60.06% were noted under same conditions. Hence, the efficiencies of the materials under the same conditions were as follows: BC-800 (1:1) > BC-800 (1:0.5) > BC-800 (1:0.25), elegantly demonstrating that dye uptake positively correlates with available surface area and pore volume.

Low dye concentrations result in fewer dye molecules in the solution, and since each molecule has a higher probability of coming into contact with the adsorbent material, removal is more effective. On the other hand, as the dye concentration rises, more dye molecules contend for the same adsorption sites on the surface, decreasing the effectiveness of dye removal. This is due to the fact that when the quantity of dye molecules rises, the adsorbent material's surface area remains constant.<sup>48,49</sup>

**3.2.4. Effect of Contact Time on Adsorption Capacity.** Contact time plays a crucial role in the dye adsorption process. Figure 5 exemplifies the effect of contact time on adsorption performance of dyes onto the adsorbent surface, and Figure S7 shows the effect of contact time on adsorption quantity. It can be seen in Figure 5a that for BC-800 (1:1) using RhB, there was rapid removal rate in the first 20 min, and the adsorption reached an equilibrium immediately after this, presenting a maximum removal of 92.60%, while BC-800 (1:0.5) and BC-800 (1:0.25) showed removal efficiencies of 86.43% and 71.82% within 40 and 150 min, respectively. For MB (Figure 5b), BC-800 (1:1) was found to have a maximum uptake of 94.51% within 15 min, while BC-800 (1:0.5) and BC-800 (1:0.25) showed maximum removals of 93.98% and 80.02% within 40 and 150 min, respectively. Similarly, for MO (Figure 5c), BC-800 (1:1), BC-800 (1:0.5), and BC-800 (1:0.25) showed their maximum uptakes of 93.23%, 91.68%, and 82.01% within 15, 30, and 50 min, respectively. BC-800 (1:1) showed the highest rate of dye removal due to its highest specific surface area and pore volume among the series of samples. For the case of RhB and MB, the maximum adsorption was achieved within 20 and 15 min faster than the most effective standard biochar without activation shown in our previous work.<sup>22</sup>

The dye solution and the adsorbent surface have a high concentration gradient at the start of the adsorption process. This causes a significant number of dye molecules to adhere to the open surface locations with a rapid initial removal rate, while the adsorption rate gradually slows down, and the equilibrium stage is reached at which the adsorbent is no longer able to uptake dye molecules onto its surface.<sup>50,51</sup>

**3.2.5. Kinetic Model Studies.** Mass transfer from the liquid phase to the adsorbent surface occurs during the physical and chemical processes of adsorption. To study the kinetics of dyes (RhB, MB, and MO), solutions with an initial concentration of 20 mg/L were used under fixed adsorbent conditions and optimal pH. The pseudo-first-order, pseudo-second-order, and

**Table 2. Pseudo-Second-Order Model and Freundlich Model Parameters Fitted to Experimental Data for Adsorption of RhB, MB, and MO onto Activated Biochars**

Samples	Dyes	Pseudo-second-order model			Freundlich model		
		R <sup>2</sup>	K <sub>2</sub> (g mg <sup>-1</sup> min <sup>-1</sup> )	Q <sub>e</sub> (mg g <sup>-1</sup> )	R <sup>2</sup>	K <sub>F</sub> (mg <sup>-1/n</sup> L <sup>1/n</sup> g <sup>-1</sup> )	n
BC-800(1:0.25)	RhB	0.9825	0.0067	12.1124	0.9792	6.9759	1.6759
	MB	0.9855	0.0012	36.5363	0.9588	14.9980	3.2599
	MO	0.9749	0.0014	93.9800	0.9909	13.0807	1.7806
BC-800(1:0.5)	RhB	0.9827	0.0069	26.3505	0.9941	12.9607	1.6912
	MB	0.9859	0.0011	86.6551	0.9442	17.2460	1.5124
	MO	0.9966	0.0021	112.3590	0.9928	24.1991	1.3877
BC-800(1:1)	RhB	0.9984	0.0188	36.0101	0.9659	28.3576	1.6208
	MB	0.9907	0.0185	96.6184	0.9927	35.7272	1.1621
	MO	0.9999	0.0166	119.7600	0.9979	10.6150	1.0259

Elovich models were used to assess their applicability on the acquired adsorption data; eqs S2, S3, and S4 show how these models were applied. The subsequent results are tabulated in Table S2 and are graphically represented in Figure S8 to present the applicability of the specific model. The highest value of the correlation coefficient R<sup>2</sup> indicates the most suitable model to explain the adsorption phenomenon. According to the data obtained through kinetics, pseudo-first-order and Elovich models did not fit well with the experiment data. However, the system exhibits a strong fit for pseudo-second-order kinetics with a high value of correlation coefficients (R<sup>2</sup>), as depicted in Table 2. In our previously reported work, the biochars without activation exhibited first-order kinetics, indicating a straightforward relationship between the rate of dye uptake and the concentration of a single reactant. This behavior suggested a primarily physical interaction with the dye molecules involved. However, following the activation process, there was a notable shift in the system's behavior. It transitioned to second-order kinetics, implying that the rate of uptake was now directly proportional to the product of the concentrations of two reagents. This confirms the chemical interaction between the activated biochars and individual dye molecules, thus resulting in the effective and rapid removal of dyes from wastewater. For BC-800 (1:1), the values of R<sup>2</sup> for pseudo-second-order kinetics are 0.9984 for RhB, 0.9907 for MB, and 0.9999 for MO. For BC-800 (1:0.5), the values are 0.9827, 0.9859, and 0.9966 for RhB, MB, and MO, respectively. Finally, for BC-800 (1:0.25), the values are 0.9925, 0.9855, and 0.9749 for RhB, MB, and MO as shown in Table 2.

The size and shape of the dye molecules are different, where RhB, MB, and MO have molecular masses of 479.02, 327.33, and 319.85 g mol<sup>-1</sup>, respectively. With this variation in molecular composition, the overall sizes of the molecules are also different where they have been measured at 1.63, 1.41, and 1.38 nm, respectively. These subtle changes in size will restrict diffusion through any micropores present in the biochars; this is compounded further as the shape and charge of the dye molecules are not the same. MO and MB have linear structures, whereas RhB has an additional branched aryl group which widens the molecule. This dye also has the capability to generate dimers, depending on the uptake environment which forms zwitter ions.<sup>45</sup> Therefore, the variation in charge states, both naturally present or induced through the pH of the solution, could retard dye diffusion and as a result limit the rate of adsorption on the surface of the

biochars. This aspect has been optimized as a full pH study has shown the most effective environment for the biochars to uptake a specific dye, shown in Figure S5.

**3.2.6. Adsorption Isotherms.** The batch method was used to investigate the relationship between the amount of dye molecules adsorbed and their equilibrium concentration in solution. The experimental data were then analyzed using the Langmuir, Freundlich, and Temkin isotherms (eqs S5, S6, and S7) to investigate the type of dye molecule adsorption on the biochars surface. The calculated values are shown in Table S3 with their isotherm plots presented in Figure S9, with corresponding data including linear plot equations in Table S4 (pseudo-first-order, pseudo-second-order, and Elovich adsorption kinetics models) and Table S5 (Langmuir, Freundlich, and Temkin adsorption isotherm models). The monolayer coverage at the adsorbent surface, which is caused by homogeneous adsorption and contains a finite number of identical sites, is described by the Langmuir model; meanwhile, multilayer coverage produced by heterogeneous adsorption of the adsorbates at the adsorbent surface is shown by the Freundlich model. The Temkin model was also studied, and it is hypothesized that as surface coverage increases, adsorption activation energy should decrease linearly.<sup>52,53</sup>

The Freundlich model, which revealed multilayer adsorption on the adsorbent surface, was found to fit the experimental data well, as evidenced by the correlation coefficients (R<sup>2</sup>) obtained from model fits in Table 2. For BC-800 (1:1), the values of R<sup>2</sup> are 0.9659 for RhB, 0.9927 for MB, and 0.9979 for MO, and for BC-800 (1:0.5), the values are 0.9941 for RhB, 0.9442 for MB, and 0.9928 for MO. For BC-800 (1:0.25), the values were found to be 0.9792 for RhB, 0.9588 for MB, and 0.9909 for MO. Additionally, the Freundlich model's component "n" is utilized to explain how favorably the kind of adsorption is, and when n > 0.5, it indicates that the adsorbate is easily adsorbed.<sup>54</sup> Table 2 demonstrates that all n values are far higher than 0.5, indicating the adsorption of dyes onto biochars in the Freundlich model was beneficial.

#### 4. FTIR AFTER ADSORPTION OF DYES

**After RhB Adsorption.** The spectra of RhB and after RhB adsorption onto the activated biochars are depicted in Figure S10a. For RhB, the appearance of peaks around 1071 and 1247 cm<sup>-1</sup> corresponds to the C–O stretching and C–N stretching, respectively. The occurrence of amino groups can be seen by the peak around 3000 cm<sup>-1</sup> which is characteristic of N–H stretching. Furthermore, the presence of a peak at 1640 cm<sup>-1</sup>

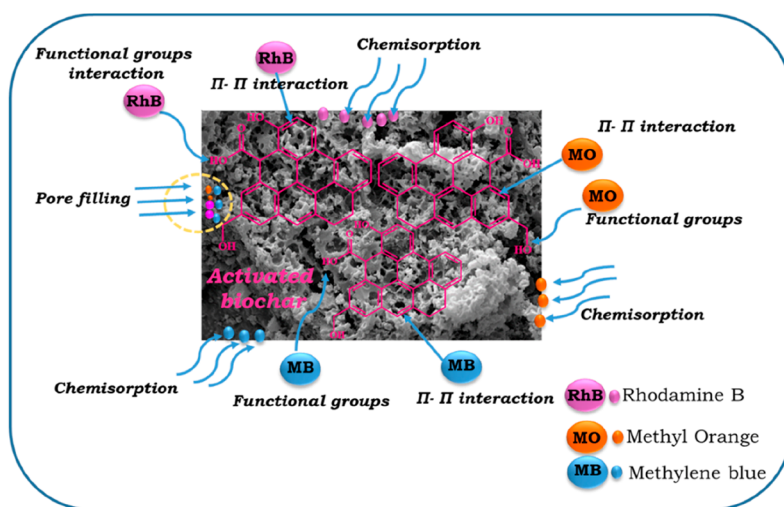


**Figure 6.** Possible adsorption routes of RhB, MB, and MO onto the surface and into the pore network of activated biochars.

points towards N–H bending due to substituted amine groups in the dye molecule.<sup>55</sup>

After adsorption, there is a shift in the position of some of the peaks; this signifies the involvement of the assigned functional groups after adsorption. The functional groups utilized in the biochar were found and identified at  $2300\text{ cm}^{-1}$  (C=O) and  $1525\text{ cm}^{-1}$  (C=C) and subtly shifted to 2293 and  $1574\text{ cm}^{-1}$  after adsorption.

**After MB Adsorption.** The spectra of MB and after adsorption of MB onto biochar are depicted in Figure S10b. The absorbance peaks at 3340, 3049, 1484, and  $1167\text{ cm}^{-1}$  were observed in the MB spectrum. The band at  $3340\text{ cm}^{-1}$  is attributed to –NH/–OH stretching vibrations. The peaks at 3049, 1484, and  $1167\text{ cm}^{-1}$  are assigned to N–H stretching, C–N stretching, and N–H bending.<sup>56</sup> The other peaks include C–S–C at  $1053\text{ cm}^{-1}$  and –CH<sub>3</sub> stretching at  $1400\text{--}1300\text{ cm}^{-1}$ .<sup>57,58</sup>

There is a shift in the positions of some bands after the adsorption of MB, which indicates the active involvement of the assigned biochar functional groups. The peaks in biochar which were at 2300 and  $1073\text{ cm}^{-1}$ , slightly shifted to 2314 and  $1093\text{ cm}^{-1}$  after MB adsorption and are assigned to C=O stretching in ketenes and C–O stretching present in the core lignin region of the biochar; these were found to decrease after adsorption of MB onto the biochar. An additional peak was observed at  $1328\text{ cm}^{-1}$  (–CH<sub>3</sub>) in the dye loaded biochars, which provides an indication of adsorption of MB dye through a methyl group.

**After MO Adsorption.** The FTIR spectra of MO and biochars after adsorption are illustrated in Figure S10c. The appearance of a peak around  $1311\text{ cm}^{-1}$  in the MO signifies the presence of S–O bonding. Peaks at 1600 and  $1516\text{ cm}^{-1}$  are characteristic for N=N stretching vibrations, and the peak at  $1362\text{ cm}^{-1}$  for C–N stretching confirms the azo nature of dye. Methyl orange displays a peak at  $2900\text{ cm}^{-1}$  for asymmetric –CH<sub>3</sub> stretching vibrations and at 817 and  $845\text{ cm}^{-1}$  for C–H bending.<sup>55,59</sup>

After adsorption of MO dye, some of the peaks observed previously in the biochars had disappeared, including the peaks at 2300 and  $1525\text{ cm}^{-1}$  assigned to C=O in ketenes and C=C stretching. The intensities of some of the peaks such as C≡C at  $2100\text{ cm}^{-1}$  and C–O at  $1060\text{ cm}^{-1}$  were also found to decrease in intensity after adsorption; this reveals the

involvement of the specific functional groups at play after adsorption.

## 5. POTENTIAL ADSORPTION PATHWAYS

The surface qualities of activated biochar, such as its specific surface area, pore size, and structure, are thought to be the most important elements in its effectiveness as an adsorbent for the removal of contaminants. In this work, wheat straw was activated using a combination of KOH introduced through a physicochemical route (sonication), followed by refluxing in HCl postpyrolysis in order to achieve meso/microporosity in the biochars. After the coral-structured biochars were generated, it was found that with three different dyes, although efficiently removed from water, the method of interaction with the biochars is different (surface adsorption through  $\pi$ – $\pi$  or hydrogen bonding); this is illustrated in Figure 6. In the case of BC-800 (1:1), having a vastly larger BET surface area and pore volume, the dye removal rate was higher indicating that pore diffusion plays a key role in the adsorption process.<sup>60</sup>

The adsorption process can be well described by the pseudo-second-order model with high values of the regression coefficient ( $R^2$ ) as shown in Table 2. Consequently, chemisorption was primarily used to modulate the behavior of the dye adsorption onto the activated biochars. Additionally, the various functional groups on the outer surfaces of activated biochar may attract dye molecules via  $\pi$ – $\pi$  interactions or H-bonding through the surface carbonyl groups identified in Figure 3. According to FTIR analysis (Figure S10a–c), RhB and MO interact with C=O and C=C groups of the activated biochars, while MB interacted with C=O and C–O groups; the three dyes all established  $\pi$ – $\pi$  stacking interactions because of their aromatic structures (Figure 6).

Adsorption kinetics demonstrated that the dyes' rate-limited adsorption process consisted of two steps: the first was a stage of gradual adsorption, and the second saw a slow down in the adsorption process due to the extremely low concentrations of dye still present in the solution.<sup>33,53</sup> Hence,  $\pi$ – $\pi$  stacking interaction, chemisorption, electrostatic interaction, and pore filling are the main mechanisms that are involved in dye adsorption onto the biochar surface.

## 6. COMPARISON WITH OTHER ADSORBENTS

The adsorption studies in this work were conducted at room temperature with a 20 mg/L initial dye concentration for all of the dyes used. For RhB and MO, the pH was kept at 6 and at 8 for MB. The prepared adsorbent can be compared to other adsorbents in the literature, both commercial and small-scale produced materials in a laboratory environment (Table S6) to reach a definite conclusion on its efficiency and applicability to real world applications, comparing specifically with other produced biorenewable adsorbents. It is evident that the surface area attained and the adsorption equilibrium time in this study are superior to those of the previously described methods of color removal from wastewater, ultimately removing a higher concentration of dye in a much shorter period of time.

## 7. REGENERATION

For an adsorbent to be truly sustainable, it must be scrutinized for its reusability, demonstrating its wider use and economic viability. To regenerate the biochars, several solvents and reagents such as NaOH, HCl, ethanol, ethanol:water solutions (ratio of 1:2), and acetone have been employed, among which absolute ethanol was found to be the most effective eluent.<sup>61,62</sup> A batch adsorption experiment was conducted with a 40 mg/L dye solution and a biochar dose of 100 mg under ambient temperature conditions. After the dye adsorption experiment, the solution was centrifuged, and the adsorbent was separated from the solution. The collected adsorbent was refluxed in 50 mL ethanol for 0.5 h, followed by washing twice with ethanol (30 mL) and dried under *vacuo*. The adsorbent was then further dried at 105 °C for 2 h to remove any moisture or EtOH residues and further used for adsorption experiments. Figure S11 illustrates the removal rate for RhB with BC-800 (1:1) at the ideal pH, which was 95.39% during the first cycle and remained at 93.11% even after the fifth cycle. According to this study, biochars can still be very stable and recyclable after multiple extraction cycles with minimal deterioration in the extraction efficiency, especially for BC-800 (1:1).

## CONCLUSIONS

In summary, we successfully synthesized activated biochars with controllable surface areas and porosities using locally abundant wheat straw waste. The high surface area and appropriate pore size make these biochars excellent candidates for removing RhB, MB, and MO dyes, achieving impressive removal efficiencies of 92.66%, 94.51%, and 93.23%, respectively, under specific conditions ( $C_0 = 20$  mg/L, dose = 6 mg, and equilibrium times of 20 min for RhB and 15 min for MB and MO). Kinetic studies favored the pseudo-second-order model ( $R^2 = 0.9984, 0.9907, \text{ and } 0.9999$  for RhB, MB, and MO). The Freundlich isotherm model highlighted chemisorption dominance, influenced by electrostatic interactions,  $\pi$ - $\pi$  stacking, and pore filling. Successful desorption allowed for efficient regeneration even after five cycles, maintaining a removal efficiency of >90% for all dyes. Activated biochars present a net zero and sustainable solution to addressing dye pollution, contributing to eco-friendly water filtration systems and advancing Sustainable Development Goal 6—ensuring clean water and sanitation for all.

## ASSOCIATED CONTENT

### Supporting Information

The Supporting Information is available free of charge at <https://pubs.acs.org/doi/10.1021/acssusresmgt.3c00109>.

Adsorption kinetic/isotherm model data and equations; UV-vis calibration plots; biochar characterization data including nitrogen physisorption, proximate, and ultimate analysis, Fourier transform infrared spectroscopy, and powder X-ray diffraction; dye removal optimization for pH and dose; adsorption quantities as a function of contact time; recyclability studies; biochar/activated carbon adsorption literature comparisons (PDF)

## AUTHOR INFORMATION

### Corresponding Author

Martin J. Taylor – School of Engineering, Chemical Engineering, University of Hull, Hull HU6 7RX, United Kingdom; [orcid.org/0000-0001-7966-6275](https://orcid.org/0000-0001-7966-6275); Email: [martin.taylor@hull.ac.uk](mailto:martin.taylor@hull.ac.uk)

### Authors

Priyanka – School of Engineering, Chemical Engineering, University of Hull, Hull HU6 7RX, United Kingdom; Department of Chemistry and Centre for Advanced Studies in Chemistry, Panjab University, Chandigarh 160 014, India

Devika Vashisht – Department of Chemistry and Centre for Advanced Studies in Chemistry, Panjab University, Chandigarh 160 014, India

Alex O. Ibhaddon – School of Engineering, Chemical Engineering, University of Hull, Hull HU6 7RX, United Kingdom

Surinder K. Mehta – Department of Chemistry and Centre for Advanced Studies in Chemistry, Panjab University, Chandigarh 160 014, India; Department of Chemistry, University of Ladakh, Kargil 194 103, India; [orcid.org/0000-0002-3560-8214](https://orcid.org/0000-0002-3560-8214)

Complete contact information is available at: <https://pubs.acs.org/10.1021/acssusresmgt.3c00109>

### Author Contributions

Conceptualization, M.J.T.; methodology, P.; formal analysis, P., D.V., and M.J.T.; investigation, P. and M.J.T.; resources, S.K.M. and M.J.T.; supervision, M.J.T. and S.K.M.; data curation, P.; writing, review and editing, P., D.V., A.O.I., S.K.M., and M.J.T. All authors contributed to the article and approved the submitted version.

### Notes

The authors declare no competing financial interest.

## ACKNOWLEDGMENTS

P., S.K.M., and M.J.T. acknowledge the Commonwealth Scholarship Commission in the United Kingdom for the award of Commonwealth Split-Site Scholarship to P. (Ref No. INCN-2022-395). P. also would like to recognize UGC, New Delhi, for a Junior Research Fellowship. We would like to thank Mr. Timothy Dunstan for the HRSEM images.

## REFERENCES

(1) Lu, F.; Astruc, D. Nanocatalysts and other nanomaterials for water remediation from organic pollutants. *Coordination Chemistry Reviews* **2020**, *408*, 213180.

- (2) Mittal, A.; Kaur, D.; Malviya, A.; Mittal, J.; Gupta, V. K. Adsorption studies on the removal of coloring agent phenol red from wastewater using waste materials as adsorbents. *J. Colloid Interface Sci.* **2009**, *337* (2), 345–354.
- (3) Han, F.; Kambala, V. S. R.; Dharmarajan, R.; Liu, Y.; Naidu, R. Photocatalytic degradation of azo dye acid orange 7 using different light sources over Fe<sup>3+</sup>-doped TiO<sub>2</sub> nanocatalysts. *Environmental Technology & Innovation* **2018**, *12*, 27–42.
- (4) Nadeem, K.; Guyer, G. T.; Dizge, N. Polishing of biologically treated textile wastewater through AOPs and recycling for wet processing. *Journal of Water Process Engineering* **2017**, *20*, 29–39.
- (5) Vinothkannan, M.; Karthikeyan, C.; Gnana kumar, G.; Kim, A. R.; Yoo, D. J. One-pot green synthesis of reduced graphene oxide (RGO)/Fe<sub>3</sub>O<sub>4</sub> nanocomposites and its catalytic activity toward methylene blue dye degradation. *Spectrochim Acta A Mol. Biomol Spectrosc* **2015**, *136*, 256–264.
- (6) Grassi, P.; Drumm, F. C.; Georjin, J.; Franco, D. S. P.; Foletto, E. L.; Dotto, G. L.; Jahn, S. L. Water treatment plant sludge as iron source to catalyze a heterogeneous photo-Fenton reaction. *Environmental Technology & Innovation* **2020**, *17*, 100544.
- (7) Roosta, M.; Ghaedi, M.; Shokri, N.; Daneshfar, A.; Sahraei, R.; Asghari, A. Optimization of the combined ultrasonic assisted/adsorption method for the removal of malachite green by gold nanoparticles loaded on activated carbon: experimental design. *Spectrochim Acta A Mol. Biomol Spectrosc* **2014**, *118*, 55–65.
- (8) Córdova, B. M.; Santa Cruz, J. P.; Ocampo M., T. V.; Huamani-Palomino, R. G.; Baena-Moncada, A. M. Simultaneous adsorption of a ternary mixture of brilliant green, rhodamine B and methyl orange as artificial wastewater onto biochar from cocoa pod husk waste. Quantification of dyes using the derivative spectrophotometry method. *New Journal of Chemistry* **2020**, *44* (20), 8303–8316.
- (9) Singh, H.; Chauhan, G.; Jain, A. K.; Sharma, S. K. Adsorptive potential of agricultural wastes for removal of dyes from aqueous solutions. *Journal of Environmental Chemical Engineering* **2017**, *5* (1), 122–135.
- (10) Liu, L.; Gao, Z. Y.; Su, X. P.; Chen, X.; Jiang, L.; Yao, J. M. Adsorption Removal of Dyes from Single and Binary Solutions Using a Cellulose-based Bioadsorbent. *ACS Sustainable Chemistry & Engineering* **2015**, *3* (3), 432–442.
- (11) Yrjälä, K.; Ramakrishnan, M.; Salo, E. Agricultural waste streams as resource in circular economy for biochar production towards carbon neutrality. *Current Opinion in Environmental Science & Health* **2022**, *26*, 100339.
- (12) Lee, J.; Yang, X.; Cho, S.-H.; Kim, J.-K.; Lee, S. S.; Tsang, D. C. W.; Ok, Y. S.; Kwon, E. E. Pyrolysis process of agricultural waste using CO<sub>2</sub> for waste management, energy recovery, and biochar fabrication. *Applied Energy* **2017**, *185*, 214–222.
- (13) Bommier, C.; Xu, R.; Wang, W.; Wang, X.; Wen, D.; Lu, J.; Ji, X. Self-activation of cellulose: A new preparation methodology for activated carbon electrodes in electrochemical capacitors. *Nano Energy* **2015**, *13*, 709–717.
- (14) Regti, A.; Laamari, M. R.; Stiriba, S.-E.; Haddad, M. E. Removal of Basic Blue 41 dyes using *Persea americana*-activated carbon prepared by phosphoric acid action. *Journal of Industrial Chemistry* **2017**, *8* (2), 187–195.
- (15) Thue, P. S.; Lima, D. R.; Lima, E. C.; Teixeira, R. A.; dos Reis, G. S.; Dias, S. L. P.; Machado, F. M. Comparative studies of physicochemical and adsorptive properties of biochar materials from biomass using different zinc salts as activating agents. *Journal of Environmental Chemical Engineering* **2022**, *10* (3), 107632.
- (16) Park, J. H.; Ok, Y. S.; Kim, S. H.; Cho, J. S.; Heo, J. S.; Delaune, R. D.; Seo, D. C. Evaluation of phosphorus adsorption capacity of sesame straw biochar on aqueous solution: influence of activation methods and pyrolysis temperatures. *Environ Geochem Health* **2015**, *37* (6), 969–983.
- (17) Hui, T. S.; Zaini, M. A. A. Potassium hydroxide activation of activated carbon: a commentary. *Carbon letters* **2015**, *16* (4), 275–280.
- (18) Li, X. Y.; Han, D.; Xie, J. F.; Wang, Z. B.; Gong, Z. Q.; Li, B. Hierarchical porous activated biochar derived from marine macroalgae wastes (*Enteromorpha prolifera*): facile synthesis and its application on Methylene Blue removal. *RSC Adv.* **2018**, *8* (51), 29237–29247.
- (19) Zhang, S.; Zheng, M.; Lin, Z.; Li, N.; Liu, Y.; Zhao, B.; Pang, H.; Cao, J.; He, P.; Shi, Y. Activated carbon with ultrahigh specific surface area synthesized from natural plant material for lithium–sulfur batteries. *J. Mater. Chem. A* **2014**, *2* (38), 15889–15896.
- (20) Raj, A.; Yadav, A.; Rawat, A. P.; Singh, A. K.; Kumar, S.; Pandey, A. K.; Sirohi, R.; Pandey, A. Kinetic and thermodynamic investigations of sewage sludge biochar in removal of Remazol Brilliant Blue R dye from aqueous solution and evaluation of residual dyes cytotoxicity. *Environmental Technology & Innovation* **2021**, *23*, 101556.
- (21) Leng, L.; Yuan, X.; Zeng, G.; Shao, J.; Chen, X.; Wu, Z.; Wang, H.; Peng, X. Surface characterization of rice husk bio-char produced by liquefaction and application for cationic dye (Malachite green) adsorption. *Fuel* **2015**, *155*, 77–85.
- (22) Priyanka; Vashisht, D.; Taylor, M. J.; Mehta, S. K. Evaluating the pre-treatment protocol required to produce an effective carbonized waste adsorbent for organic pollution control. *Frontiers in Environmental Science* **2023**, *11*, na DOI: 10.3389/fenvs.2023.1224388.
- (23) Taylor, M.; Alabdrabalemeer, H.; Skoulou, V. Choosing Physical, Physicochemical and Chemical Methods of Pre-Treating Lignocellulosic Wastes to Repurpose into Solid Fuels. *Sustainability* **2019**, *11* (13), 3604.
- (24) Wang, P.; Wu, C.; Guo, Y.; Wang, C. Experimental and theoretical studies on methylene blue and methyl orange sorption by wheat straw-derived biochar with a large surface area. *Phys. Chem. Chem. Phys.* **2016**, *18* (43), 30196–30203.
- (25) Qu, J.; Wang, Y.; Tian, X.; Jiang, Z.; Deng, F.; Tao, Y.; Jiang, Q.; Wang, L.; Zhang, Y. KOH-activated porous biochar with high specific surface area for adsorptive removal of chromium (VI) and naphthalene from water: Affecting factors, mechanisms and reusability exploration. *J. Hazard Mater.* **2021**, *401*, No. 123292.
- (26) Quan, C.; Gao, N.; Song, Q. Pyrolysis of biomass components in a TGA and a fixed-bed reactor: Thermochemical behaviors, kinetics, and product characterization. *Journal of Analytical and Applied Pyrolysis* **2016**, *121*, 84–92.
- (27) Danish, M.; Naqvi, M.; Farooq, U.; Naqvi, S. Characterization of South Asian Agricultural Residues for Potential Utilization in Future ‘energy mix’. *Energy Procedia* **2015**, *75*, 2974–2980.
- (28) Subratti, A.; Vidal, J. L.; Lalgee, L. J.; Kerton, F. M.; Jalsa, N. K. Preparation and characterization of biochar derived from the fruit seed of *Cedrela odorata* L and evaluation of its adsorption capacity with methylene blue. *Sustainable Chemistry and Pharmacy* **2021**, *21*, 100421.
- (29) Acosta, R.; Fierro, V.; Martinez de Yuso, A.; Nabarlantz, D.; Celzard, A. Tetracycline adsorption onto activated carbons produced by KOH activation of tyre pyrolysis char. *Chemosphere* **2016**, *149*, 168–176.
- (30) Taylor, M. J.; Alabdrabalemeer, H. A.; Michopoulos, A. K.; Volpe, R.; Skoulou, V. Augmented Leaching Pretreatments for Forest Wood Waste and Their Effect on Ash Composition and the Lignocellulosic Network. *ACS Sustainable Chem. Eng.* **2020**, *8* (14), 5674–5682.
- (31) Xu, J.; Zhang, Y.; Li, B.; Fan, S.; Xu, H.; Guan, D. X. Improved adsorption properties of tetracycline on KOH/KMnO<sub>4</sub> modified biochar derived from wheat straw. *Chemosphere* **2022**, *296*, No. 133981.
- (32) Yang, X.; Kwon, E. E.; Dou, X.; Zhang, M.; Kim, K. H.; Tsang, D. C. W.; Ok, Y. S. Fabrication of spherical biochar by a two-step thermal process from waste potato peel. *Sci. Total Environ* **2018**, *626*, 478–485.
- (33) Fu, Y.; Shen, Y.; Zhang, Z.; Ge, X.; Chen, M. Activated biochars derived from rice husk via one- and two-step KOH-catalyzed

pyrolysis for phenol adsorption. *Sci. Total Environ* **2019**, *646*, 1567–1577.

(34) Dehkhoda, A. M.; Gyenge, E.; Ellis, N. A novel method to tailor the porous structure of KOH-activated biochar and its application in capacitive deionization and energy storage. *Biomass and Bioenergy* **2016**, *87*, 107–121.

(35) Abbaci, F.; Nait-Merzoug, A.; Guellati, O.; Harat, A.; El Haskouri, J.; Delhalle, J.; Mekhalif, Z.; Guerioune, M. Bio/KOH ratio effect on activated biochar and their dye based wastewater depollution. *Journal of Analytical and Applied Pyrolysis* **2022**, *162*, 105452.

(36) Rodriguez, J. A.; Lustosa Filho, J. F.; Melo, L. C. A.; de Assis, I. R.; de Oliveira, T. S. Influence of pyrolysis temperature and feedstock on the properties of biochars produced from agricultural and industrial wastes. *Journal of Analytical and Applied Pyrolysis* **2020**, *149*, 104839.

(37) Md Salim, R.; Asik, J.; Sarjadi, M. S. Chemical functional groups of extractives, cellulose and lignin extracted from native *Leucaena leucocephala* bark. *Wood Science and Technology* **2021**, *55* (2), 295–313.

(38) Adeniyi, A. G.; Abdulkareem, S. A.; Iwuzor, K. O.; Ogunniyi, S.; Abdulkareem, M. T.; Emenike, E. C.; Sagboye, P. A. Effect of salt impregnation on the properties of orange albedo biochar. *Cleaner Chemical Engineering* **2022**, *3*, 100059.

(39) Reza, M. S.; Afroze, S.; Bakar, M. S.A.; Saidur, R.; Aslfattahi, N.; Taweekun, J.; Azad, A. K. Biochar characterization of invasive *Pennisetum purpureum* grass: effect of pyrolysis temperature. *Biochar* **2020**, *2* (2), 239–251.

(40) Li, Y.; Xing, B.; Wang, X.; Wang, K.; Zhu, L.; Wang, S. Nitrogen-Doped Hierarchical Porous Biochar Derived from Corn Stalks for Phenol-Enhanced Adsorption. *Energy Fuels* **2019**, *33* (12), 12459–12468.

(41) Shen, Y.; Fu, Y. KOH-activated rice husk char via CO<sub>2</sub> pyrolysis for phenol adsorption. *Materials Today Energy* **2018**, *9*, 397–405.

(42) Chintala, R.; Mollinedo, J.; Schumacher, T. E.; Papiernik, S. K.; Malo, D. D.; Clay, D. E.; Kumar, S.; Gulbrandson, D. W. Nitrate sorption and desorption in biochars from fast pyrolysis. *Microporous and Mesoporous Materials* **2013**, *179*, 250–257.

(43) Stratton, B. C.; Pierre, A. J.; Riser, E. A.; Grinals, N. J.; Edwards, C. W.; Wohlwend, A. M.; Bauer, J. S.; Spera, R. J.; Pferdmenges, L. S.; Griffith, K. M.; et al. Synthesis and Optical Characterization of a Rhodamine B Spirolactam Dimer. *J. Phys. Chem. A* **2022**, *126* (26), 4211–4220.

(44) Yin, M.; Pan, Y.; Pan, C. Adsorption properties of graphite oxide for Rhodamine B. *Micro & Nano Letters* **2019**, *14* (11), 1192–1197.

(45) Thabede, P. M.; Shooto, N. D.; Naidoo, E. B. Removal of methylene blue dye and lead ions from aqueous solution using activated carbon from black cumin seeds. *South African Journal of Chemical Engineering* **2020**, *33*, 39–50.

(46) Yildirim, S.; Isik, B.; Ugraskan, V. Methyl orange dye sequestration using polyaniline nanotube-filled sodium alginate bio-composite microbeads. *Materials Chemistry and Physics* **2023**, *307*, 128083.

(47) Consiglio Kasemodel, M.; Romão, E. L.; Bueno Ruiz Papa, T. Adsorption of methylene blue on babassu coconut (*Orbignya speciosa*) mesocarp commercial biochar. *International Journal of Environmental Science and Technology* **2024**, *21*, 1671.

(48) Ogunlusi, G. O.; Amos, O. D.; Olatunji, O. F.; Adenuga, A. A. Equilibrium, kinetic, and thermodynamic studies of the adsorption of anionic and cationic dyes from aqueous solution using agricultural waste biochar. *Journal of the Iranian Chemical Society* **2023**, *20* (4), 817–830.

(49) Ravindiran, G.; Jeyaraju, R. M.; Nandipati, G.; Seerangounder, S.; Al-Zaqri, N.; Boshala, A.; Hayder, G. Prevention of groundwater contamination from the pollutants released from dyeing industries using biochar produced from palm shell. *Urban Climate* **2023**, *49*, 101515.

(50) Sterenzon, E.; Vadivel, V. K.; Gerchman, Y.; Luxbacher, T.; Narayanan, R.; Mamane, H. Effective Removal of Acid Dye in Synthetic and Silk Dyeing Effluent: Isotherm and Kinetic Studies. *ACS Omega* **2022**, *7* (1), 118–128.

(51) Basu, S.; Ghosh, G.; Saha, S. Adsorption characteristics of phosphoric acid induced activation of bio-carbon: Equilibrium, kinetics, thermodynamics and batch adsorber design. *Process Safety and Environmental Protection* **2018**, *117*, 125–142.

(52) Liu, L.; Lin, Y.; Liu, Y.; Zhu, H.; He, Q. Removal of Methylene Blue from Aqueous Solutions by Sewage Sludge Based Granular Activated Carbon: Adsorption Equilibrium, Kinetics, and Thermodynamics. *Journal of Chemical & Engineering Data* **2013**, *58* (8), 2248–2253.

(53) Chen, S.; Qin, C.; Wang, T.; Chen, F.; Li, X.; Hou, H.; Zhou, M. Study on the adsorption of dyestuffs with different properties by sludge-rice husk biochar: Adsorption capacity, isotherm, kinetic, thermodynamics and mechanism. *Journal of Molecular Liquids* **2019**, *285*, 62–74.

(54) Kallel, F.; Chaari, F.; Bouaziz, F.; Bettaieb, F.; Ghorbel, R.; Chaabouni, S. E. Sorption and desorption characteristics for the removal of a toxic dye, methylene blue from aqueous solution by a low cost agricultural by-product. *Journal of Molecular Liquids* **2016**, *219*, 279–288.

(55) Braham Dutt Arya, N. M. FTIR Spectroscopic Analysis of Various Pharmaceutically Important Organic Dyes. *World Wide Journal of Multidisciplinary Research and Development* **2015**, *1* (5), 48–52.

(56) Xia, Y.; Yao, Q.; Zhang, W.; Zhang, Y.; Zhao, M. Comparative adsorption of methylene blue by magnetic baker's yeast and EDTAD-modified magnetic baker's yeast: Equilibrium and kinetic study. *Arabian Journal of Chemistry* **2019**, *12* (8), 2448–2456.

(57) Alshehri, A. A.; Malik, M. A. Biogenic fabrication of ZnO nanoparticles using *Trigonella foenum-graecum* (Fenugreek) for proficient photocatalytic degradation of methylene blue under UV irradiation. *Journal of Materials Science: Materials in Electronics* **2019**, *30* (17), 16156–16173.

(58) Uddin, M. K.; Nasar, A. Walnut shell powder as a low-cost adsorbent for methylene blue dye: isotherm, kinetics, thermodynamic, desorption and response surface methodology examinations. *Sci. Rep.* **2020**, *10* (1), 7983.

(59) Cyril, N.; George, J. B.; Joseph, L.; Syllas, V. P. Catalytic Degradation of Methyl Orange and Selective Sensing of Mercury Ion in Aqueous Solutions Using Green Synthesized Silver Nanoparticles from the Seeds of *Derris trifoliata*. *Journal of Cluster Science* **2019**, *30* (2), 459–468.

(60) Li, P.; Zhao, T.; Zhao, Z.; Tang, H.; Feng, W.; Zhang, Z. Biochar Derived from Chinese Herb Medicine Residues for Rhodamine B Dye Adsorption. *ACS Omega* **2023**, *8* (5), 4813–4825.

(61) Singh, N.; Riyajuddin, S.; Ghosh, K.; Mehta, S. K.; Dan, A. Chitosan-Graphene Oxide Hydrogels with Embedded Magnetic Iron Oxide Nanoparticles for Dye Removal. *ACS Applied Nano Materials* **2019**, *2* (11), 7379–7392.

(62) Manipady, S. R.; Singh, A.; Basavaraja, B. M.; Samal, A. K.; Srivastava, S.; Saxena, S. Iron–Carbon Hybrid Magnetic Nanosheets for Adsorption-Removal of Organic Dyes and 4-Nitrophenol from Aqueous Solution. *ACS Applied Nano Materials* **2020**, *3* (2), 1571–1582.